

## RESEARCH ARTICLE

10.1002/2016JB013765

## Key Points:

- Independent component analysis is appropriate for exploratory analysis of InSAR data
- Deformation can be identified automatically by cluster analysis of independent components
- Application of ICA demonstrated on Sentinel-1A imagery using contrasting volcanic examples

## Supporting Information:

- Supporting Information S1

## Correspondence to:

S. K. Ebmeier,  
s.k.ebmeier@leeds.ac.uk

## Citation:

Ebmeier, S. K. (2016), Application of independent component analysis to multitemporal InSAR data with volcanic case studies, *J. Geophys. Res. Solid Earth*, 121, 8970–8986, doi:10.1002/2016JB013765.

Received 16 NOV 2016

Accepted 23 NOV 2016

Accepted article online 25 NOV 2016

Published online 16 DEC 2016

## Application of independent component analysis to multitemporal InSAR data with volcanic case studies

S. K. Ebmeier<sup>1</sup>
<sup>1</sup>School of Earth and Environment, University of Leeds, Leeds, UK

**Abstract** A challenge in the analysis of multitemporal interferometric synthetic aperture radar (InSAR) data is distinguishing and separating volcanic, tectonic, and anthropogenic displacements from each other and from atmospheric or orbital noise. Independent component analysis (ICA) is a method for decomposing a mixed signal based on the assumption that the component sources are non-Gaussian and statistically independent. ICA has potential as a tool for exploratory analysis of InSAR data, and in particular for testing whether geophysical signals are related or independent. This article presents tests of the applicability of ICA to InSAR by using synthetic data and application to Sentinel-1A archive images from two contrasting examples of volcano deformation. Coeruptive subsidence associated with the April 2015 eruption of Calbuco (Chile) was identified in spatial patterns found by maximizing both spatial and temporal independence. Spatial patterns and rates of lava subsidence were retrieved by using ICA analysis of interferograms from Parícutin lava fields (México) and found to be consistent with previous observations. I demonstrate that ICA is an appropriate method for the analysis of volcanic signals in the presence of atmospheric noise and propose a strategy for the reliable identification of geophysical displacements by using cluster analysis of the spatial patterns of independent components. This approach allows the detection of geophysical processes on a range of scales and provides a test of signal independence where multiple displacement sources are active.

## 1. Introduction

Interferometric synthetic aperture radar (InSAR) allows centrimetric to millimetric movement of the ground to be measured on the scale of tens to hundreds of kilometers at a spatial resolution of less than tens of meters and temporal resolution of days to months [e.g., Bürgmann *et al.*, 2000; Simons and Rosen, 2007]. InSAR measurements have been used to measure deformation during all stages of the earthquake cycle [Massonnet *et al.*, 1993; Elliott *et al.*, 2016] and to observe a broad range of processes that cause deformation at volcanoes [Pinel *et al.*, 2014; Biggs *et al.*, 2014].

Here I present an application of a blind source separation method, independent component analysis (ICA), for identifying and analyzing displacement signals in InSAR data. I describe the potential of the method, already widely used in other branches of remote sensing, medical physics, and geophysics, for application to multitemporal InSAR data (section 2). I demonstrate its application by using sets of synthetic interferograms (section 3.1) and analyze two contrasting styles of volcanic deformation by using Sentinel-1 imagery acquired since the instrument's launch in 2014 (section 3.2).

## 1.1. Mixed Signals: Atmospheric and Geophysical Signals

A major challenge for using InSAR for the measurement of geophysical signals is the separation of true surface displacements from atmospheric noise [e.g., Zebker *et al.*, 1997; Beauducel *et al.*, 2000]. Atmospheric signals in interferograms are the consequence of differences in the refractivity of the atmosphere between satellite acquisitions caused by variations in concentrations of water vapor ("wet delay") and hydrostatic pressure ("dry delay") [e.g., Hanssen, 2001]. Where the atmosphere is stratified, changes to water vapor concentration are correlated with topography and may mask deformation signals with similar or lower magnitude at high relief faults and at volcanoes [e.g., Doin *et al.*, 2009; Poland and Lu, 2004; Ebmeier *et al.*, 2013]. Where turbulent mixing is dominant, atmospheric signals are spatially correlated on the scale of tens of kilometers [e.g., Lohman and Simons, 2005].

Atmospheric signals can be mitigated in sets of interferograms by using approaches that increase the signal-to-noise ratio. For example, stacking a set of  $m$  independent interferograms reduces the standard deviation of

signals uncorrelated in time by a factor of  $\sqrt{m}$  [Emardson *et al.*, 2003]. This approach is very effective for estimating constant rates of deformation in the presence of turbulent atmospheric signals but does not mitigate the effect of stratified water vapor signals, which are not random in space and may not be sampled evenly across the seasons [Doin *et al.*, 2009]. Atmospheric signals are spatially but not temporally correlated, so can be estimated by high-pass filtering in time and low-pass filtering in space [Ferretti *et al.*, 2001; Hooper *et al.*, 2007]. Both stacking of repeat acquisitions and spatiotemporal filtering are most effective where deformation is of much longer duration than the measurement interval (satellite repeat time), but less effective for deformation captured by only a few interferograms, such as some landslides or coeruptive volcanic deformation.

Atmospheric signals can be **corrected in individual interferograms either empirically** [e.g., Wicks *et al.*, 2002] **or using independent predictions or measurements of water vapor and hydrostatic pressure**, and therefore atmospheric phase delays [e.g., Jolivet *et al.*, 2011]. Empirical correction removes the part of the phase caused by stratified water vapor variation by characterizing the relationship between phase delay and topographic height. This may assume a linear [e.g., Elliott *et al.*, 2008] or nonlinear [e.g., Remy *et al.*, 2003] relationship between phase and topography, which it may be necessary to characterize on different spatial scales across an interferogram [e.g., Bekaert *et al.*, 2015]. Model predictions of atmospheric delay may be derived from regional atmospheric models [e.g., Parker *et al.*, 2015] or nested models that allow higher-resolution predictions at the site of interest (e.g., over Big Island, Hawai'i [Foster *et al.*, 2006]). Interpolated measurements of atmospheric parameters from GPS networks or multispectral satellite data can be used to reduce the contribution of atmospheric delays by themselves or in combination with model predictions [e.g., Walters *et al.*, 2013]. The success of such data and model-based correction depends on (1) the availability and relative spatial density of atmospheric data or model prediction grid spacing, (2) the relative timing of InSAR and atmospheric data acquisitions, and (3) model initialization conditions [Foster *et al.*, 2013; Jolivet *et al.*, 2014; Parker *et al.*, 2015].

The correction of atmospheric phase contributions is particularly difficult over topography that varies on a short spatial scale, for example, in measuring the slip rate of major faults [e.g., Elliott *et al.*, 2008; Doin *et al.*, 2009]. Volcanic settings introduce additional challenges for both empirical and predictive atmospheric mitigation, as high topography can induce turbulence on the scale of kilometers, and volcanic plumes may also contain water vapor [e.g., Wadge *et al.*, 2016].

In some settings, it is common for multiple deformation processes to be superimposed in interferograms. For example, interferograms spanning the period after a large earthquake are likely to capture displacements associated with large aftershocks, postseismic processes, and landsliding. Variations in hydrological loading, fault creep, and anthropogenic deformation may occur in the same area over longer time scales and mask the presence of lower magnitude processes. At an active volcano, multiple related or independent processes often result in simultaneous surface displacements, including magma movement, magma phase changes, small earthquakes, and the postemplacement adjustment of erupted pyroclastic flows, lahars, and lavas [e.g., Jay *et al.*, 2014; Caricchi *et al.*, 2014; Ebmeier *et al.*, 2014]. Where a deformation source has been well characterized, it can be subtracted before modeling [e.g., González *et al.*, 2012]. If temporal and spatial characteristics of any of a set of superimposed sources are known, it may also be possible to separate signals empirically, in a similar manner to the methods for mitigating spatially correlated atmospheric noise.

ICA provides a tool for **exploratory analysis of mixed signals in interferograms and a robust test for signal independence**. It is complementary to mitigating atmospheric or deformation signals using modeling or empirical correction and requires very limited a priori assumptions about signal characteristics.

## 1.2. Independent Component Analysis

Independent component analysis (ICA) is a computational signal processing method that aims to describe random variables as a linear combination of statistically independent components [e.g., Comon, 1994; Hyvärinen and Oja, 1997; Stone, 2004]. This is achieved by the decomposition of a mixed signal using the assumption that each constituent component has a non-Gaussian probability distribution. This assumption is based on the premise that the sum of a sufficient number of non-Gaussian probability distributions tends toward a Gaussian distribution (the central limit theorem), so that a strongly non-Gaussian component is unlikely to be produced by a combination of different sources.

The assumption of statistical independence employed by ICA makes it possible to find a unique solution to the decomposition of a mixed signal, in a similar way that the assumption that sources are uncorrelated is the basis of principal component analysis (PCA). Because ICA retrieves sources by maximizing statistical independence (rather than signal variance, as in PCA) it is appropriate for the extraction of low-magnitude signals, even where noise is high, without a priori assumptions beyond the independence of the components [Hyvärinen *et al.*, 2004]. Statistical independence is assessed by non-Gaussianity. This can be quantified by using different properties of the random variables, of which kurtosis and negentropy are widely used. Kurtosis describes the relative contribution of extreme deviations to a probability distribution ("tailedness") and is normally measured as the absolute value of the fourth standardized moment of the data, with a Gaussian distribution taking a value of 3. The calculation of kurtosis is simple, but in practice, it is more sensitive to outliers than negentropy, which is more widely used for ICA. Negentropy is a concept from information theory that describes the difference in entropy—a measure of the unpredictability of information content—relative to the Gaussian distribution of the same mean and variance. This is based on the result that a Gaussian distribution has the highest value of entropy of all the possible random variables with the same variance. To avoid the challenging estimation of the probability density function, most algorithms use an approximation of negentropy to assess Gaussianity [e.g., Hyvärinen and Oja, 2000].

Figure 1 illustrates the application of ICA and PCA to a simple one-dimensional example. Three simple independent signals (Figure 1a) are combined in different ratios to produce signal mixtures (Figure 1b) that are more Gaussian than each of the individual input signals (and therefore have higher values of kurtosis). The mixed signals are decomposed to find three principal components (PCs; Figure 1c), identified so that they account for as much of the variability of the mixed signals as possible, and three independent components (ICs; Figure 1d), that maximize the statistical independence of the components. Although the PCs capture major features of the input signals (e.g., compare input "a" to PC2), each PC contains contributions from all three input signals. The ICs are successful in retrieving the structure of the original inputs, although they are not identical (e.g., compare IC1 to input "b"), and their signs and magnitudes are ambiguous (e.g., the sign of IC3 is the opposite of input "c").

ICA allows the decomposition of a mixed signal into a set of linear, additive components. For a set of  $m$  scalar mixed signals (rows of data matrix,  $\mathbf{X}$ ), with  $n (\leq m)$ , unknown statistically independent components (rows of source matrix,  $\mathbf{S}$ ), the linear relationship between the two can be described as  $\mathbf{X} = \mathbf{A} \mathbf{S}$  (1), where the rows of the unknown mixing matrix,  $\mathbf{A} (m \times n)$  are coefficients that describe the relative contribution of each source to a particular mixed signal (Figure 2). Each independent component is then estimated by choosing unmixing vectors that maximize the non-Gaussianity of its product with the data, assessed by using a property such as kurtosis or negentropy (the specific approach taken by the FastICA algorithm used in this study is described further in section 2.1). Because both  $\mathbf{A}$  and  $\mathbf{S}$  are unknown, a scaling factor in one of the components could always be canceled out by its inverse factor in the mixing matrix, so the sign and the variance (and therefore the true magnitude) of independent components are ambiguous [Hyvärinen and Oja, 2000]. However, the part of the signal that is of interest (or the original mixed signal itself) can be reconstructed as the outer product of the relevant rows of  $\mathbf{A}$  and  $\mathbf{S}$ .

ICA has been applied in medical physics, e.g., to blood oxygen level-dependent signals in functional magnetic resonance imaging used to identify connectivity in brain structures [Beckmann and Smith, 2004; Calhoun and Adali, 2006]. For this application many specialized ICA tools have been developed. Satellite remote sensing applications include hyperspectral unmixing [Bayliss *et al.*, 1998], cloud masking [Amato *et al.*, 2008], and thermal hot spot detection [Barnie and Oppenheimer, 2015]. ICA has also been used to analyze various geophysical and geochemical data sets including Global Positioning System time series [Liu *et al.*, 2015], seismic data [De Lauro *et al.*, 2009], and isotopic data [Iwamori and Albarède, 2008].

## 2. Method

### 2.1. Application of ICA to InSAR

ICA can be used to decompose mixed signals that are a linear combination of statistically independent components. As each pixel in an interferogram can be thought of as the sum of particular points in time series of various noise and deformation sources, the assumption of linear mixing is appropriate for InSAR data. Interferograms are formed by multiplying a first SAR radar image ("master") point wise by the complex

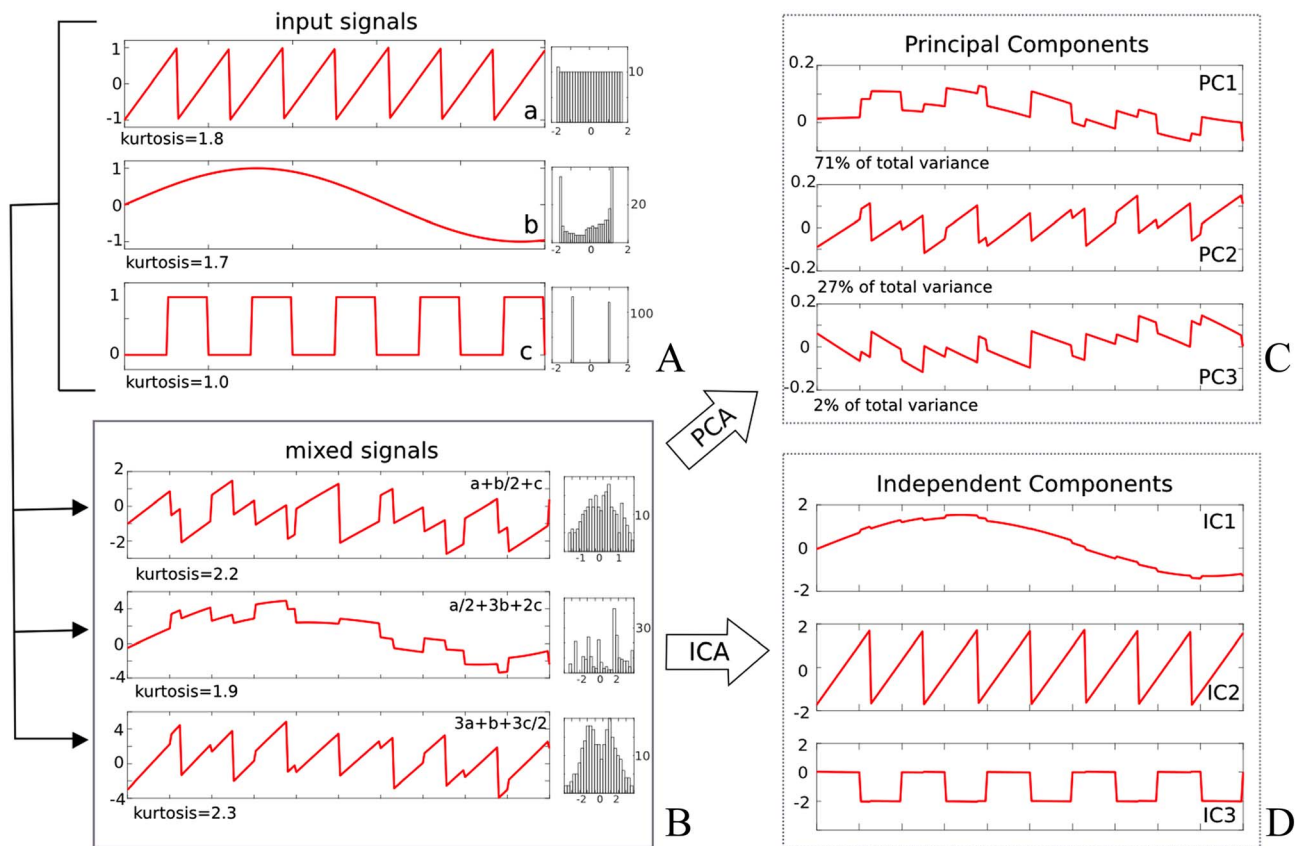


**Figure 1.** One-dimensional illustration of the application of PCA and ICA to mixed signals. (a) Three simple input signals (a, b, and c) are combined in different ratios to produce (b) three mixed signals. Histograms show the distribution of values for the whitened (zero mean, variance = 1) inputs or signal mixtures. The mixed signals are decomposed into (c) principal components and (d) independent components.

conjugate of a second image (“slave”) to produce a map of phase change. If the phase backscattered from the Earth’s surface is constant, then the interferogram phase ( $\phi$ ) between two time-separated radar images consists of the linear combination of all of the differences in propagation phase from various temporally and spatially varying sources:  $\phi = \phi_{\text{def}} + \phi_{\text{atm}} + \phi_{\text{noise}} + \Delta\phi_{\text{orbit}}$ , where  $\phi_{\text{def}}$  is the phase change due to the displacement of the Earth’s surface in the direction of the satellite’s line of sight, and other sources of phase change are normally treated as nuisance factors. A geometric contribution to phase change from the satellite’s change in position is corrected from imperfect knowledge of satellite position and the Earth’s topography, leaving just residual phase contributions from errors in knowledge of satellite position and look angle ( $\Delta\phi_{\text{orbit}}$ ). Thermal noise ( $\phi_{\text{noise}}$ ) is generally expected to be low magnitude and is neglected, while differences in atmospheric path delay between the two images ( $\phi_{\text{atm}}$ ) may be of similar or equal magnitude to geophysical signals. For much InSAR data these noise and deformation sources are expected to be statistically independent in space and/or time, although correlations between deformation and atmospheric signals may occur in some circumstances (section 1.1).

For a spatiotemporal data set, ICA requires that sources are statistically independent in either space or in time (Figure 2). For spatial ICA (sICA), spatial independence is maximized, and the number of mixed signals is the same as the number of interferograms ( $m$ ), each sampled at many thousands of points ( $n_{\text{pixel}}$ ). Phase contributions from errors in the estimation of orbital contributions, instrument noise, turbulent atmospheric variation, and displacement are all expected to be spatially independent. Deformations caused by different stages of the earthquake cycle, anthropogenic, hydrological, and various volcanic processes all have distinctive spatial distributions [e.g., González et al., 2012; Pinel et al., 2014; Elliott et al., 2016]. However, both variations in a stratified atmosphere and deformation at volcanoes and major faults are often correlated with topography [e.g., Remy et al., 2003; Doin et al., 2009] and therefore each other. When tropospheric phase delay is

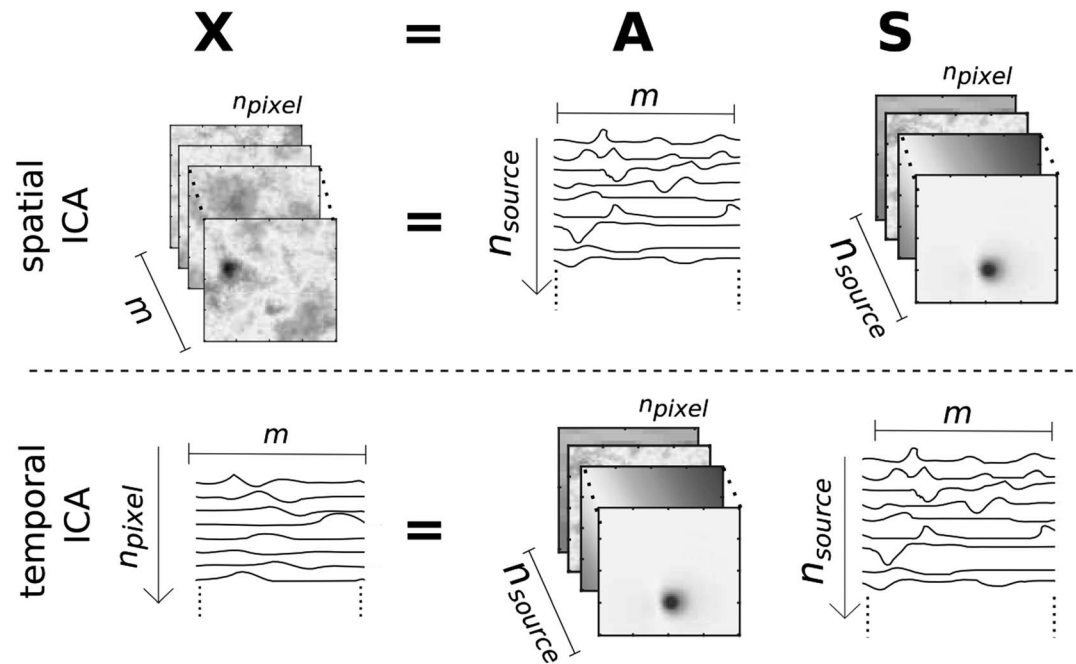


**Figure 2.** Cartoon illustrating the geometry of decomposition for a multitemporal InSAR data set,  $\mathbf{X}$ , with  $m$  interferograms, each made up of  $n_{\text{pixel}}$  pixels. For sICA, rows of the mixing matrix,  $\mathbf{A}$ , capture the relative contribution of each independent spatial component (rows of  $\mathbf{S}$ ). For tICA, spatial patterns are retrieved in the rows of  $\mathbf{A}$ , while independent temporal components are retrieved in rows of  $\mathbf{S}$ .

limited to the part of an interferogram where deformation is occurring, the assumption that sources are spatially independent may be incorrect.

Alternatively, one can assume that signal sources are statistically independent in time, so that each mixed signal is the time series for one pixel ( $n_{\text{pixel}}$  mixed signals, sampled in each interferogram). Temporal ICA (tICA) is intuitively appealing, because we expect the time series of atmospheric variation and deformation caused by different processes to be independent. However, for whole interferograms (e.g., 10–100 km footprint and pixel size of approximately tens of meters) it is computationally much more challenging than sICA, because conditioning the mixed signals for analysis requires the computation of a covariance matrix of the order of  $n_{\text{pixel}}^2$ , where  $n_{\text{pixel}}$  may be 1000–10,000.

If a set of interferograms is used to estimate phase on  $m$  epochs, the matrix of observations,  $\mathbf{X}$ , will have dimensions  $n_{\text{pixel}} \times m$ , where  $n_{\text{pixel}}$  is the number of pixels with phase data for every epoch (Figure 2). ICA decomposes the mixed signals into a set of  $n_s$  statistically independent sources in the rows of source matrix,  $\mathbf{S}$  (sICA:  $n_s \times n_{\text{pixel}}$ ; tICA:  $n_s \times m$ ) and mixing vectors in the rows of mixing matrix  $\mathbf{A}$  (sICA:  $n_s \times m$ ; tICA:  $n_s \times n_{\text{pixel}}$ ). Here this is achieved by using a fast fixed-point algorithm for ICA (FastICA) [Hyvärinen and Oja, 1997; Hyvärinen and Oja, 2000]. The first steps of this algorithm are the centring and whitening of observations before processing so that the mixing matrix is orthogonal, reducing the number of free parameters. This is achieved by subtracting the mean from mixed signal matrix,  $\mathbf{X}$ , so that the observations are zero mean variables. The mixed signals are then transformed linearly to be expressed in terms of uncorrelated variables of variance equal to 1 (whitening or sphering). The FastICA algorithm achieves this by preconditioning the centered observations using PCA, which can additionally be used to reduce noise in the data. The number of principal components retained for the ICA analysis should be lower than the data dimensionality (which is unknown for most real data), so I use a trial and error approach to select an appropriate number [e.g., Barrie and Oppenheimer, 2015]. A reasonable starting point can be found by making a rough estimation of the number of independent spatial or temporal sources expected for a particular number of interferograms. For spatial ICA, a good starting point is one less than the dimension of the data (number of interferograms), since the spatially correlated atmosphere that appears in every interferogram is independent in time. As orbital and turbulent atmospheric contributions are uncorrelated in time, these contribute only Gaussian noise in



time and will not be extracted as independent components in temporal ICA [e.g., Hyvärinen and Oja, 2000]. The number of independent temporal sources is therefore likely to be much lower than the dimension of the data (number of pixels) and should be reduced to an estimation of the number of temporally correlated processes occurring in the area being analyzed. This initial estimation can be iteratively increased so that as many PCs as possible are retained without introducing overfitting (identified by sources that are isolated peaks in the ICs retrieved [e.g., Hyvärinen et al., 1999]).

The whitened (potentially reduced dimension) data matrix ( $\mathbf{Z}$ ) is found by multiplying  $\mathbf{X}$  by a whitening matrix,  $\mathbf{V}$ , so that  $\mathbf{Z} = \mathbf{V}\mathbf{X} = \mathbf{V}\mathbf{A}\mathbf{S} = \tilde{\mathbf{A}}\mathbf{S}$ , where  $\tilde{\mathbf{A}}$  is an adjusted orthogonal mixing matrix. The problem is thus reframed in terms of the whitened data  $\mathbf{Z} = \tilde{\mathbf{A}}\mathbf{S}$ , so that approximation of  $\tilde{\mathbf{A}}^{-1}$  is an unmixing matrix,  $\mathbf{W}$ , which can be used to estimate the source matrix,  $\mathbf{S}$ , from the whitened data,  $\mathbf{Z}$ .

The FastICA algorithm estimates unmixing matrix,  $\mathbf{W}$ , by using a fixed-point iteration—where each point in a converging sequence is a function of the previous one. Each row of  $\mathbf{W}$  is an unmixing vector,  $\mathbf{w}$ , that represents a projection of the centered and whitened data ( $\mathbf{Z}$ ) to maximize non-Gaussianity as measured using an approximation of negentropy [Hyvärinen and Oja, 2000]. For each unmixing vector, the iteration is initiated from a random value for  $\mathbf{w}$  and repeated until estimations converge (that is,  $\mathbf{w}_{\text{new}}, \mathbf{w}_{\text{old}} \sim 1$ ). Independent components are extracted one by one, with the projections of previously identified mixing vectors ( $\mathbf{w}_1 \dots \mathbf{w}_n$ ) subtracted from the next mixing vector ( $\mathbf{w}_{n+1}$ ), which is orthogonalized relative to all the mixing vectors identified so far. If the fixed-point iteration failed to converge, then the number of independent components extracted was reduced to be one less than the number of principal components.

The source matrix,  $\mathbf{S}$ , is then estimated from  $\mathbf{W}\mathbf{Z}$ , and the relative contributions of the source in  $\mathbf{S}$  to each pixel (tICA) or time point (sICA) are then  $\mathbf{V}^{\text{inv}}\mathbf{W}^{-1} (\sim \mathbf{A})$ , where  $\mathbf{V}^{\text{inv}}$  is an approximate inverse of the whitening matrix. Detailed explanations of the FastICA algorithm are provided by Hyvärinen and Oja [1997] and Hyvärinen and Oja [2000].

## 2.2. Identifying and Testing the Significance of Deformation Signals

If the spatial or temporal characteristics of a deformation sign are known, then the source can be identified by visual inspection of the independent components or mixing matrix. However, because FastICA uses random starting points in the estimation of each row of the unmixing matrix,  $\mathbf{w}$ , independent components are retrieved in different orders on different runs of the algorithm, so that it is difficult to extract the component of interest automatically. This requires either a priori information about the location or timing of the target deformation signal, or a test of the statistical significance of the retrieved independent sources. Testing the statistical significance of sources is important for exploratory analysis of InSAR data and also provides greater flexibility for identifying undescribed or poorly constrained deformation signals.

Testing whether independent components capture real aspects of the data can be achieved by randomizing input data in some way (e.g., bootstrapping) and repeating the retrieval of independent components from different starting points (e.g., FastICA's initial guesses for each row of  $\mathbf{W}$ ). Independent components that are retrieved by multiple runs are likely to represent a true property of the data [Hyvärinen, 2013]. A better alternative is to compare the spatial patterns in the independent components or mixing matrices retrieved from ICA of independent groups of data [e.g., Esposito et al., 2005]. In this study, I used the ISCTEST algorithm [Hyvärinen and Ramkumar, 2013], developed to examine intersubject or intersession consistency in a neuroimaging context. ISCTEST uses an empirical model of the null distribution of independent components, that is, for the case where components of different groups of data are no more similar than would be expected by chance. Although the ISCTEST algorithm was developed for neuroimaging applications, the empirical model of the null distribution is based only on the assumption that independent components from the same data sets can be described as part of the same multivariate distribution that captures the spatial patterns of both signal and noise in the data, with parameters estimated from observations (the algorithm is explained in detail by Hyvärinen and Ramkumar [2013]). The empirical estimation of the null distribution is used to estimate the probability that the intergroup similarity of two sources arises at random.  $P$  values for intergroup similarity can then be used to identify clusters of similar components.

The division of InSAR data sets into independent groups can be conducted systematically or at random, depending on the characteristics of the source(s) of interest. For example, if deformation is thought to persist throughout the whole period of observation, then the data set can be divided into two blocks of

interferograms spanning separate, sequential periods of time. For short-lived deformation, it may be preferable to randomly divide all acquisition dates into two separate groups and construct two independent sets of interferograms spanning similar total time periods.

### 3. Results

#### 3.1. Tests With Synthetic Data

I constructed sets of simple synthetic interferograms with similar average properties to those derived from Sentinel-1 SAR data (Figure 3). These included an emulation of spatially correlated atmosphere [e.g., Hanssen, 2001; Lohman and Simons, 2005], tropospherically correlated atmospheric variations [e.g., Remy et al., 2003], and linear ramps (of the form  $ax+by+c$ , where  $a \sim b \sim 0.01 \text{ km}^{-1}$ ), representing errors in the estimation of orbits). I used central values of maximum variance =  $20 \text{ mm}^2$  and characteristic length-scale exponent = 0.5, after Emardson et al. [2003], and assumed a normal distribution to randomly generate spatially correlated atmosphere for each synthetic image. Sample Shuttle Radar Topography Mission (SRTM) topography of footprint  $1600 \text{ km}^2$ , encompassing Osorno volcano (2652m, Southern Chile), was used to generate stratified atmospheric signals with an average phase delay gradient of  $1 \text{ cm/km}$  [e.g., Bekaert et al., 2015]. Interferogram phase screens were then estimated by adding together the spatially and topographically correlated atmospheric phase for each image and differencing sequential images. Orbital contributions and a synthetic line-of-sight deformation signal were then added to each interferogram.

Synthetic deformation patterns were constructed by evaluating a Mogi model at 5 km depth in an elastic half-space for (a) a linear increase in source volume over time, (b) sinusoidal variations in source volume (c) a "pulsed" episode of source deflation spanning just a few interferograms ( $<1$  month), and (d) a "step" in deformation captured in just one interferogram. A Mogi source [Mogi, 1958] was selected for simplicity, and because it provides a reasonable first-order approximation of a variety of time-varying deformation sources including magmatic/hydrothermal reservoirs or the withdrawal of groundwater. The deformation source was located beneath the topography for Osorno volcano, with a second deformation source located northwest of the volcano for some tests.

The final synthetic data therefore consists of a set of "daisy chain" interferograms of  $40 \times 40 \text{ km}$  dimensions,  $\sim 500 \text{ m}$  pixel size (to limit computation time), and 12 day separation, referenced to the first image acquisition time (Figure 3). These synthetic data are simpler than real interferograms and do not include, for example, nonlinear phase-topography gradients, quadratic orbital ramps, or any loss in image coherence. However, they do capture the primary features of an InSAR data set sufficiently well to test the applicability of ICA for source separation.

I applied the ICA methodology described above to examine the impact of varying (1) the number of synthetic interferograms used as input data, (2) signal-to-noise ratio of the deformation source, and (3) temporal characteristics of the deformation source. Tests using temporal rather than spatial ICA were conducted on down-sampled versions of the same synthetic data of 20 by 20 pixels (size 2 km); to reduce the size of the covariance matrix it was necessary to estimate. To test the significance of the independent components retrieved by using the clustering method described above (section 2.2), synthetic data sets with the same deformation sources, but different random noise, were produced in pairs.

The success of ICA in analyzing the synthetic InSAR data can be assessed for two different aims. First, the ICs should capture the spatial and temporal characteristics of the input signals sufficiently well for them to be useful in exploring the development of and relationships between different deformation signals. I use the clustering method for identifying real sources (described in section 2.2) as a test for whether ICs contain useful information. A second aim is the accurate reconstruction of the original input deformation signal in a form suitable for modeling. Such reconstruction will be most successful when input sources are very non-Gaussian. The presence of Gaussian noise and correlations between input signals in space (sICA) or time (tICA) result in signals caused by different processes being captured in the same independent components and introduce noise to any reconstructed interferograms.

Clusters containing the ICs that captured the spatial pattern of input deformation were identified from sICA for even very small synthetic data sets ( $<5$  interferograms). For tICA, clusters capturing input deformation patterns were most reliably identified for larger data sets ( $>20$  interferograms). For small sample sizes (i.e.,

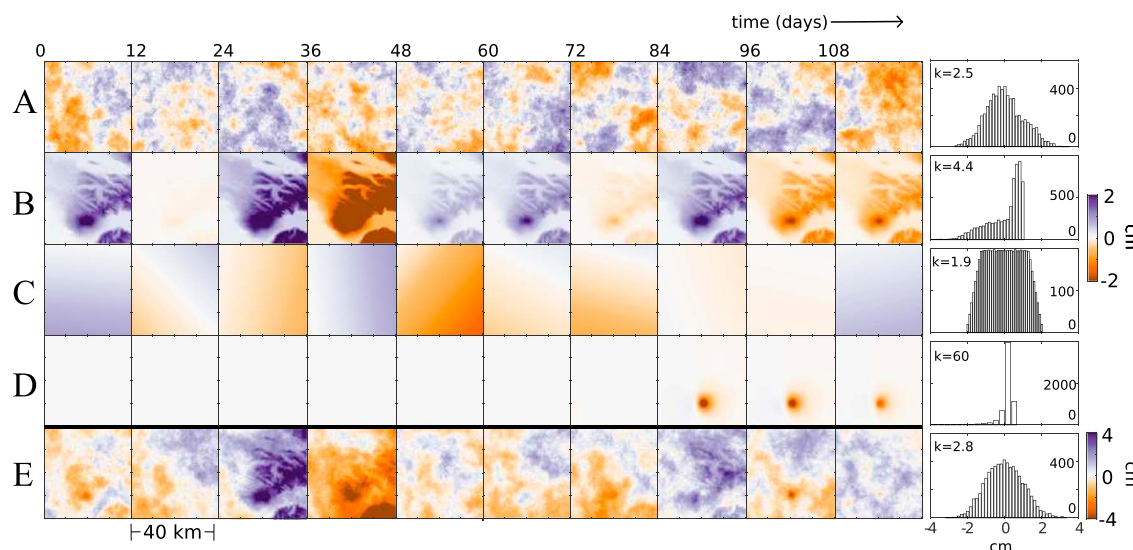


**Figure 3.** The signals used to construct a set of synthetic interferograms. (a) Spatially correlated atmospheric phase contribution, (b) topographically correlated atmospheric delay, and (c) linear orbital ramps of the form  $\phi = ax + by + c$ , where  $a$  and  $b$  are normally distributed randomly generated numbers with central values of  $\sim 0.01 \text{ km}^{-1}$ . (d) Synthetic deformation—in this case a Mogi source at 5 km depth, for short-lived episode of inflation starting on day 75. (e) Synthetic interferograms, from the sum of signals in Figures 3a–3d. Histograms show the distribution of values for the last interferogram in the sequence (days 108–120).

tens of interferograms, relative to 10,000s of pixels) ICA algorithms are less stable, and if too many principal components are retained, also prone to overfitting.

For all the different input deformation styles, clusters of ICs were identified for signal-to-noise ratio (SNR)  $> 0.1$ . For lower signal-to-noise ratios, deformation was sometimes removed during dimension reduction before performing the ICA. Deformation was only lost at very low SNR for sICA, where usually only the smallest eigenvector had been removed. As dimension reduction is a more important prerequisite to tICA, the successful identification of clusters was more sensitive to SNR, and for the examples examined here, was more successful at SNR  $> 0.5$ .

The residuals between interferograms reconstructed from the clustered component and the original input deformation are also sensitive to SNR for some types of deformation. Figure 4 illustrates the variation of root-mean-square (RMS) residuals in relation to the SNR of the synthetic data for sICA (SNR is approximated as the ratio of maximum deformation to maximum noise). For a pulse of deformation, RMS residuals level out to a value of  $\sim 0.2 \text{ cm}$  at SNR  $> 1$ , but are 3 times higher where SNR  $< 1$ . For linear displacements, RMS residuals vary across a range of almost  $\sim 0.5 \text{ cm}$  without obvious dependence on input SNR.

Identical deformation sources or those where the volume change of one source was a function of the other in time (i.e., coupled sources) were retrieved in the same independent component, provided that episodes of deformation were sufficiently long relative to the satellite repeat time (e.g., appeared in  $> 2$  interferograms). Deformation events limited to just one interferogram always appear to be independent of other sources. Independent deformation sources, such as the example shown in Figure 5a, were retrieved as separate components (Figure 5b), making it possible to separate them into different sets of reconstructed interferograms (Figure 5d).

For paired groups of synthetic interferograms (same deformation source characteristics with randomly generated atmospheric and orbital sources) intergroup clusters of components consistently retrieve the input deformation (e.g., clusters shown in Figure 5c). However, when the look angle is changed for the two different groups to represent a comparison of ascending and descending data, then statistically significant intergroup clusters are only found for near vertical deformation, as the horizontal components of displacement seen by the satellite are more sensitive to look angle. For the synthetic data used here, independent components containing atmospheric features were also assigned to clusters in about 10% of cases, normally where synthetic interferograms were dominated by topographically correlated atmospheric delay. These false positives present a challenge for automation but were easily identified by eye and may be exacerbated by the simple representation of atmospheric signals in the synthetic data.



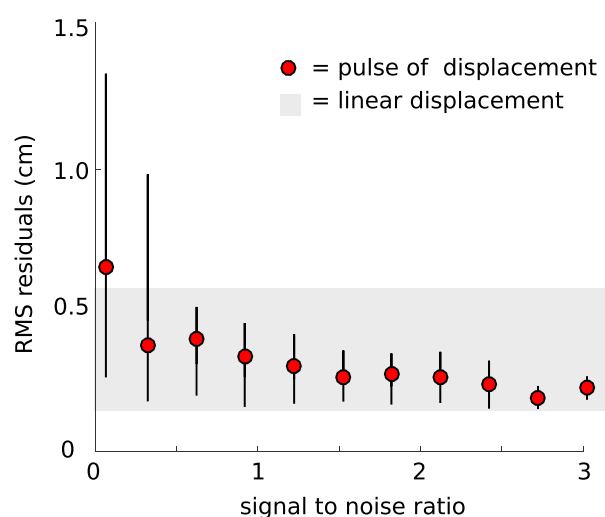


**Figure 4.** Variation of root-mean-square (RMS) residuals (cm) in relation to the SNR of the input synthetic data for interferograms reconstructed from a single IC identified by sICA.

### 3.2. Application to Volcanic Displacements With Sentinel-1 SAR Data

I used interferograms spanning two recent periods of contrasting volcanic deformation from the archive of Sentinel-1a imagery to investigate the applicability of ICA. Given that Sentinel-1 will provide the largest, freely available SAR data set over the coming decades, it provides the most useful test for the applicability of ICA to real data. Volcanic deformation is a reasonable “proof-of-concept” test, because deformation rates were in both cases high enough to be detectable in the 18 months of imagery acquired since Sentinel-1A's launch in 2014. The two examples investigated represent end-members for temporal characteristics of volcano deformation detectable using InSAR. The only deformation to have been detected at Calbuco volcano, Chile, was during an eruption in April 2015, while lava flows at Parícutin, México, have been subsiding steadily for decades. Subsidence at Calbuco was high in magnitude ( $\sim 12$  cm), clearly identifiable in a single interferogram, and therefore provides a clear illustration of how ICs representing deformation can be identified. In contrast, deformation is not immediately obvious in any one individual interferogram from Parícutin but can be identified from the products of ICA.

#### 3.2.1. Data Processing and Preparation

SAR images from the European Commission's Sentinel-1A satellite were used to construct a set of interferograms over two volcanoes (Parícutin, México, and Calbuco, Chile) and processed using GAMMA software ([www.gamma-rs.ch](http://www.gamma-rs.ch)). Images were acquired in Terrain Observation by Progressive Scans mode, and coregistration of master and slave single-look complex images was achieved by iterative estimation of constant range and azimuth offsets from cross correlation and then from Doppler variation in burst overlap regions [e.g., González *et al.*, 2015]. Topographic phase contributions were corrected by using Shuttle Radar Topography Mission (SRTM) 30 m data [Farr *et al.*, 2007]. Interferograms were unwrapped by using a minimum cost flow method and were processed at 12 and 2 looks in range and azimuth, respectively, to give a pixel size of approximately 30 m.

#### 3.2.2. Coeruptive Subsidence at Calbuco, Chile

Calbuco volcano in Southern Chile erupted on 22 April 2015, 54 years after its last major eruption. The ash plume reached heights of up to 18 km and ejected  $\sim 4.5 \pm 2.3 \times 10^{11}$  kg tephra [Romero *et al.*, 2016; Van Eaton *et al.*, 2016]. No deformation was detected in the weeks before the onset of the eruption in Sentinel-1A InSAR data or during regional InSAR surveys that covered the Southern Andes between 2006 and 2010 [Fournier *et al.*, 2010; Pritchard *et al.*, 2013]. Interferograms from three separate tracks do capture coeruptive subsidence of  $\sim 12$  cm, which appears to have occurred only during the first two phases of the eruption on the 22–23 April. Here I use daisy-chain Sentinel-1 interferograms from a single track (164) that spans the Calbuco eruption. The timespan of most interferograms is 24 days, but there was a significant gap in acquisitions between June and November 2015 that resulted in one interferogram spanning 168 days.

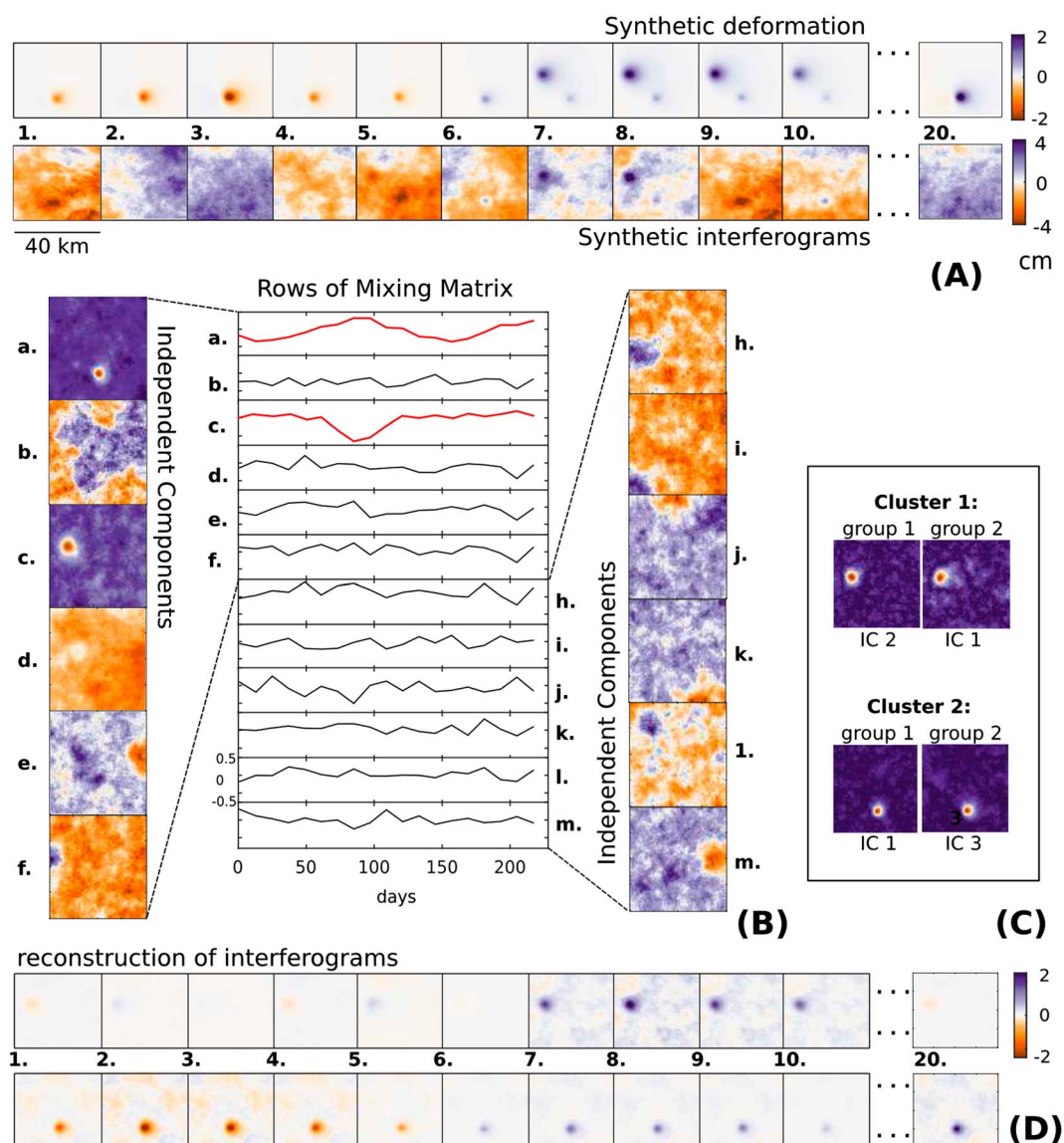


**Figure 5.** Illustration of workflow for analysis of a synthetic set of interferograms capturing two independent deformation sources. (a) Synthetic deformation for a Mogi-type source at 5 km depth with sinusoidal variations in volume (lower source) and a second source at 7 km depth inflating for ~1 month (upper source in time steps 7–10). Synthetic interferograms include atmospheric and orbital contributions as well as deformation and are expressed in terms of satellite line-of-sight displacement. (b) Independent spatial components of the set of interferograms, shown with letters to match the corresponding rows of the mixing matrix, which show the contribution of each spatial component to each interferogram in the synthetic data set. (c) Clusters of independent components from the analysis shown in Figure 5b and a similar set of randomly generated interferograms. The  $P$  values for the components being parts of the same cluster are 0.8 and 0.7 for sources 1 and 2, respectively. (d) Reconstruction of interferograms showing the two independent synthetic deformation sources identified from cluster analysis, calculated as the outer product of the relevant rows of the mixing and sources matrices.

Spatial ICA was performed on a subset of the Sentinel-1A interferograms of dimensions  $\sim 50 \times 50$  km. Twelve interferograms (Table S1 in the supporting information) were used in the analysis, and the data dimensions were reduced to 10 during preparation and whitening. No atmospheric corrections or temporal filtering was performed on the data set before application of ICA. To use tICA on the same data, I downsampled the subset by a factor of 10 to ease computation time and similarly reduced the dimension of the data to 10 during whitening.

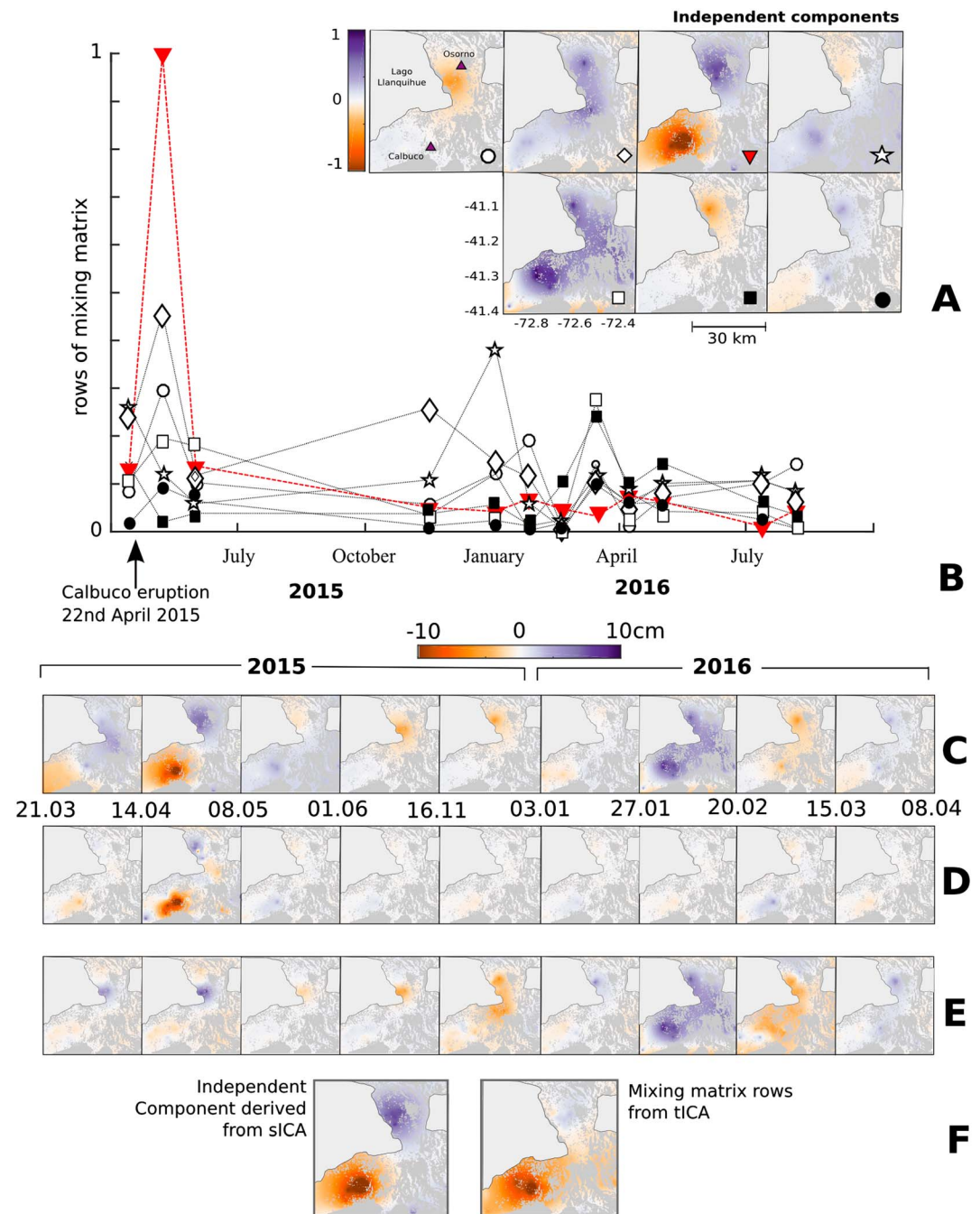


**Figure 6.** (a) Selection of independent components from ICA of a set of 12 interferograms spanning the time between 21 March 2015 and 6 August 2016 (505 days) over Calbuco volcano, Chile. The colors are scaled between  $-1$  and  $1$  for presentation. (b) Mixing matrix rows for the components shown in Figure 6a, plotted against the slave date of each interferogram, and scaled between  $0$  and  $1$ . Each point shows the relative contribution of the corresponding spatial pattern shown in Figure 6a to a single interferogram in the data set. (c) Interferograms used for the analysis (first 9 of the full set of 12). Numbers below show the date of the master image for the reconstructed interferogram to the right (dd.mm). (d) Interferograms reconstructed from the independent spatial components and mixing matrix rows identified as deformation. (e) Interferograms reconstructed from the independent spatial components and mixing matrix rows not associated with deformation, and instead considered to be dominated by atmospheric features. (f) Comparison of spatial patterns of the independent spatial component (from sICA) and the mixing matrix row (from tICA).

A selection of independent spatial components and mixing matrix rows from the sICA analysis is shown in Figure 6, with the one associated with co-eruptive deformation marked by a red triangle. Note that this IC also

captures an atmospheric feature at Osorno volcano. Other components are consistent with topographically correlated atmospheric signals, for example, the black circle or the white square in Figures 6a and 6b, which show signals associated with both Osorno and Calbuco volcanoes and contribute to the phase observed in many of the interferograms. The mixing matrix rows (Figure 6b) show the relative contributions of the spatial components to each interferogram in the analysis.

As deformation only appears in one of the sequential daisy-chain interferograms, the interferograms were reconstructed to create two independent groups without any acquisition dates in common, so that each group included one interferogram that spanned the eruption (group 1: 20150321–20150508 and group 2: 20150414–20150601). The ICs containing the deformation from the two groups were identified as a cluster ( $p$ -value=0.76).

Interferograms containing just the components associated with deformation were reconstructed by taking the outer product of the relevant mixing and source matrix rows. These reconstructed interferograms (Figure 6d) are dominated by the coeruptive subsidence in the interferogram that spanned the 22–23 April eruption, although there is also some residual noise spread through the other reconstructed interferograms. This noise gives an indication of the expected level of uncertainty in the reconstruction of the coeruptive deformation field ( $<2$  cm) and is much lower than the variance of the interferograms reconstructed from the remaining components ( $\sim 5.5$  cm; Figure 6e). The spatial patterns associated with coeruptive deformation derived from sICA and tICA are compared in Figure 6f. They are similar (but not identical) over Calbuco, but quite different over Osorno volcano.

### 3.2.3. Lava Subsidence of the Parícutin Lava Fields

In 1943 a new monogenetic cone, Parícutin, appeared in a cornfield in the Michoacán-Guanajuato volcanic field in central México. Over the next 9 years  $1.9 \text{ km}^3$  [Fries, 1953] of basaltic-andesitic lavas and pyroclastic products were deposited over an area of  $\sim 25 \text{ km}^2$  in around 40 separate lava flows with a total thickness exceeding 200 m. The Parícutin lava flows have now been subsiding for over 60 years and past InSAR observations up to 2011 detected linear subsidence at a rate of up to  $\sim 5 \text{ cm/yr}$  [Fournier *et al.*, 2010; Chaussard, 2016]. Lavas were erupted from a cinder cone onto what had previously been gently sloping farmland, so in this case deformation signals are not expected to be strongly correlated with topography.

I performed sICA on interferograms from both ascending and descending tracks of Sentinel-1A imagery (Table S1) to test whether the already well-characterized spatial patterns of deformation are captured as an independent component. For both data sets the number of dimensions were reduced during preconditioning to one less than the number of interferograms, and the same number of independent components was retrieved. The usefulness of ICA was tested at two scales: first for a subset of the interferogram  $40 \times 40 \text{ km}$  and second for a smaller subset ( $\sim 5 \text{ km} \times 5 \text{ km}$ ) over the lavas themselves. Although lava subsidence can be identified in one of the independent components estimated from the  $40 \times 40 \text{ km}$  subset, their spatial patterns are seen more clearly in the  $5 \times 5 \text{ km}$  extract shown in Figure 7. Although lava subsidence is not clearly visible in many of the input interferograms due to the relatively low signal-to-noise ratio in any single time period (Figure 7a), both tracks of data are decomposed to produce an independent component with a spatial pattern that closely matches patterns of lava subsidence described by other authors (Figure 7b). Specifically, the signal maximum appears in the same location ( $\sim -102.242^\circ, 19.499^\circ$ ) in components from both ascending and descending data sets (Figures 7c and 7d), and in the same location as where Chaussard [2016] measured maximum subsidence over the thickest part of the 1943–1952 lava flow. Furthermore, three distinct patches of subsidence are captured in the same independent component from the ascending (151) track of data and are associated with a less distinct patch in the descending (114) data. The three signal patches are caused by the same physical process (the cooling and compaction of lavas emplaced  $>60$  years ago), which is consistent with them being retrieved within the same independent component. The differences in the deformation retrieved from the two tracks are primarily due to the differences in their total temporal coverage (i.e., lower magnitude deformation is detected only over a longer period).

By separating the Parícutin data for each track into two independent groups, I tested whether the component containing the deformation could be identified automatically. As we can expect lava subsidence so long after emplacement to have a constant rate over the 1.5 years over which Sentinel-1A acquired data, I divided the interferograms into two sequential groups, removing the midpoint interferogram so that the groups did not



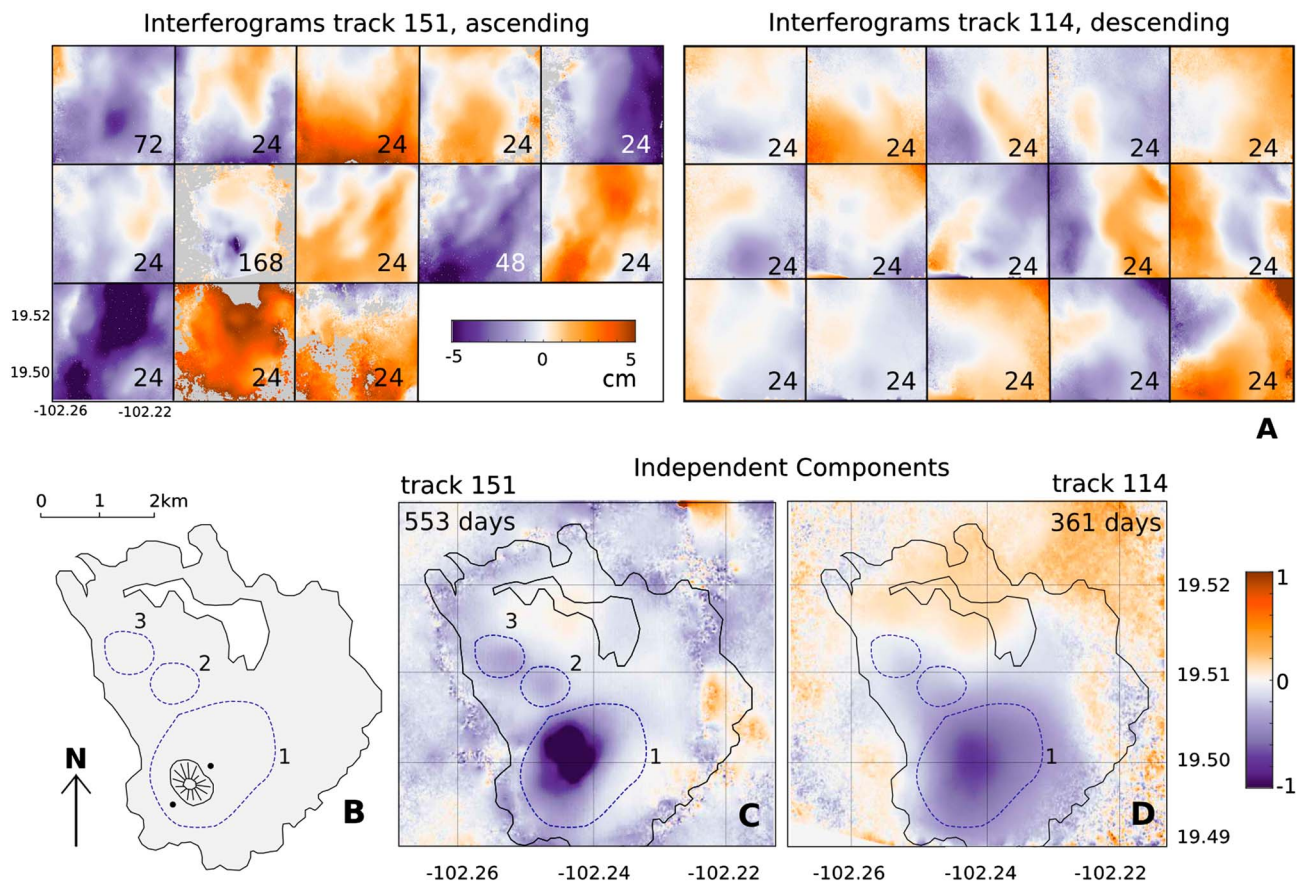


**Figure 7.** (a) Interferograms used in ICA analysis of InSAR signals over Parícutin lava fields from ascending and descending tracks of Sentinel-1A data (numbers in corners refer to number of days spanned by the interferogram). (b) Spatial extent of Parícutin lava fields (in grey [after *Chaussard*, 2016]) with the location of deformation measured in ALOS interferograms (2007–2011) indicated by blue dashed outlines. The location of the cinder cone built up between 1943 and 1952 is marked along with two secondary eruptive vents (black circles). (c) Spatial pattern of an independent component capturing lava subsidence found from spatial ICA of 13 Sentinel interferograms (track 151, ascending) spanning the period between 27 December 2014 and 1 July 2016. (d) Spatial pattern of an independent component capturing lava subsidence found from spatial ICA of 15 interferograms (track 114, descending) spanning the period between 29 May 2015 and 23 May 2016. As the magnitudes of independent components are ambiguous [e.g., *Hyvärinen and Oja*, 2000], they are scaled here between 1 and –1 for presentation purposes.

hold any acquisition dates in common. The central long-period 168 day interferogram was also removed from the analysis of track 151 so that it did not dominate the independent components retrieved. Although no clusters between the two independent groups were identified with the desired confidence (false positive rate for the existence of a cluster and false discovery rate of an independent component belonging to a cluster set to  $<5\%$  [after *Hyvärinen and Ramkumar*, 2013]), the pair of components with the greatest probability ( $p=0.5$ ) of capturing the same feature were those with the same spatial pattern as the lava subsidence (the two independent components identified as a cluster for track 151 are shown in Figure S1 in the supporting information). Although the lava flow subsidence is not clear in any of the interferograms spanning  $<100$  days, ICA is able to retrieve the largest displacement signal from both tracks of images, and even the smaller, lower magnitude lobes of subsidence in the ascending track, which spanned a longer time period.

I reconstructed interferograms from the ascending track IC that captures the lava subsidence field and estimated a linear subsidence rate from the total cumulative displacement over the whole time period. Region 1 (Figure 7b) is subsiding at  $5.3\text{ cm/yr} \pm 0.5\text{ cm/yr}$  (in line of sight), with the uncertainty taken as the variance of the reconstructed interferograms in areas away from the lava fields. This is close to the value of  $5.5\text{ cm/yr}$  found by *Chaussard* [2016] between 2007 and 2011. Estimations of the rate of subsidence for the two smaller patches are, however, slower than previous measurements, being  $1.5 \pm 0.5\text{ cm/yr}$  in 2014–2016 relative to  $3.3\text{ cm/yr}$  in 2007–2011.

#### 4. Discussion

ICA has potential as a tool for exploratory analysis of InSAR data sets, automatically identifying displacements, assessing the relationships between deformation signals, and in some circumstances, for separating displacements from atmospheric noise. It is likely to be particularly useful for interrogating the large volumes of satellite radar imagery now available for monitoring geophysical signals.

As an analysis tool, ICA will be particularly useful, where a priori information about deformation location or temporal characteristics is limited. Deformation sources that do not share a causal mechanism are likely to result in independent displacement patterns, and as such will be decomposed into separate ICs. In contrast, deformation related to the same physical process will be captured by the same IC, as seen at the Parícutin lavas, where three separate patches of subsidence appear in the same independent component (Figures 7c and 7d).

Exploratory analysis requires a reliable method for assessing the statistical significance of the ICs. I found that cluster analysis of ICs from different groups was reliable for automatically extracting the IC related to input deformation from tests with synthetic data at  $\text{SNR} > 0.1$ . The ICs associated with lava subsidence at Parícutin had the highest probability ( $p=0.5$ ) of being an intergroup cluster for two groups of 6–7 interferograms, as did the ICs that capture co-ruptive deformation at Calbuco ( $p=0.76$ ). Although the examples presented here are both volcanic, a very similar approach could be used to analyze deformation associated with tectonic or anthropogenic processes, landsliding or for searching for transient events, such as small earthquakes, or seasonal hydrological loading. Separating otherwise similar interferograms into independent groups requires redundancy in the number of satellite acquisitions and will be most successful where either deformation is constant and long-lived relative to satellite repeat time (of days) or coherence is sufficiently good to allow multiple (probably longer timespan) interferograms to be formed over the period of interest. An alternative method may be to look for correlations between independent components retrieved from recent interferograms and either past deformation signals or the a priori expected location of deformation. Qualitative comparison of ICs retrieved from sICA and tICA of the same data sets may also be useful, although the properties of ICs that are independent in space versus independent in time may be different (e.g., as at Calbuco; Figure 6f).

For the mitigation of atmospheric artefacts, predictive methods are theoretically preferable to empirical approaches, such as ICA. However, as their efficacy depends on the density and quality of independent atmospheric data available, or the resolution and initial conditions of an atmospheric model, there are some situations where an empirical approach is likely to provide better results. ICA may also be suitable for initial “quick-look” analyses of large data sets before atmospheric data or higher-resolution models can be prepared. At Calbuco, for example, it was possible to remove much of the atmospheric signal from the time series with sICA without the use of any independent atmospheric data, although the discrepancy between spatial patterns extracted with sICA and tICA suggests that some contribution from topographically correlated atmosphere is likely to remain. An additional application of sICA could be the identification and removal of quasi-systematic features in phase, not directly correlated with topography, but associated with regular meteorological patterns (e.g., as observed at Medicine Lake [Parker et al., 2015]). ICA is a complementary approach to temporal filtering, which can be done as a preparatory step [e.g., Hyvärinen and Oja, 2000]. It is also more flexible than spatiotemporal filtering for the identification (and potentially extraction) of short-lived deformation signals captured in just a few interferograms (e.g., section 3.2.2).

Deformation that is spatially correlated with atmospheric signals, for example, at steep, isolated volcanoes, could potentially result in both features being encompassed in the same spatial IC. However, stratified water vapor signals are normally spread throughout an interferogram rather than limited specifically to the location of deformation, and as such are part of a broad (if discontinuous) spatial pattern. For example, atmospheric signals at Calbuco are commonly accompanied by similar signals at neighboring Osorno and are decomposed into the same IC (Figure 6). However, deformation captured by only a single interferogram in a time series (as at Calbuco) is particularly challenging to separate from tropospheric atmospheric features based on either spatial or temporal independence, and ICs from both approaches contain contributions from atmospheric signals (Figure 6f).

ICA generally requires the assumption that no more than one of the independent components can be Gaussian, because any orthogonal transformation of independent Gaussian variables will have the same

multivariate distribution [e.g., Hyvärinen and Oja, 2000]. Where atmospheric signals are likely to have a Gaussian distribution in space or more likely in time, adaptations to the methodology presented here [e.g., Beckmann and Smith, 2004] could improve the quality of the results. Further advances in ICA methodology that can be applied to InSAR data include the simultaneous maximization of spatial and temporal independence and the use of skewed rather than symmetrical probability density functions [e.g., Stone et al., 2002].

## 5. Conclusions

ICA is an appropriate and useful method for the analysis of multitemporal InSAR data, and especially for the exploratory analysis of geophysical signals.

Tests with synthetic interferograms indicate that the characteristics of input deformation sources can be retrieved by maximizing either the spatial or temporal independence of source components and that independent deformation sources are extracted into separate components. By splitting input data into two independent groups, the source component containing deformation can be identified reliably by using cluster analysis. This allows for the automatic identification, and potentially also reconstruction, of deformation.

Coeruptive deformation over Calbuco (Chile) in April 2015 was identifiable in the spatial patterns derived from both spatial and temporal ICA of 12 Sentinel interferograms, although there were differences between the two approaches. Atmospheric contributions were reduced in interferograms reconstructed from the spatial component containing deformation but were not removed entirely. In particular, the spatial component describing deformation probably encompassed some signals associated with topographically correlated atmosphere.

An analysis of 29 Sentinel-1A interferograms over Parícutin lava flows (México) using sICA captures the shape of three distinct patches of lava subsidence as part of the same spatial component, consistent with deformation caused by a common process. Lava subsidence rates estimated from the reconstructed signal are consistent with previous InSAR measurements of deformation.

These prototype examples demonstrate that the combination of ICA and cluster analysis is appropriate for the analysis of InSAR data and that it has potential for (1) identifying geophysical signals caused by tectonic, volcanic, or anthropogenic processes and (2) testing the independence of geophysical signals.

## Acknowledgments

This research was supported by a European Space Agency Living Planet Fellowship (IMRICA) (from April 2015, School of Earth Sciences, University of Bristol) and by the Leverhulme Trust through a Leverhulme Early Career Fellowship to SKE (from May 2016, School of Earth and Environment, University of Leeds). S.K.E. would like to thank the Department of Earth Sciences at the University of Oxford for visitor status 2013–2015 and the Centre for the Observation and Modelling of Earthquakes, Volcanoes and Tectonics for providing computing facilities and for cofunding the European Space Agency Fellowship while at the University of Bristol (April 2015 to April 2016). The FastICA and ISCTEST software are available from webpages of the Aalto University ([research.ics.aalto.fi/ica/software.shtml](http://research.ics.aalto.fi/ica/software.shtml)) and the University of Helsinki, Finland ([www.cs.helsinki.fi/u/ahyvairin/code/isctest/](http://www.cs.helsinki.fi/u/ahyvairin/code/isctest/)). Sentinel-1A interferograms are derived works of Copernicus data (2015), and the Sentinel-1a images analyzed here can be obtained from <https://scihub.copernicus.eu/dhus/>.

## References

- Amato, U., A. Antoniadis, V. Cuomo, L. Cutillo, M. Franzese, L. Murino, and C. Serio (2008), Statistical cloud detection from SEVIRI multispectral images, *Remote Sens. Environ.*, 112(3), 750–766, doi:10.1016/j.rse.2007.06.004.
- Barnie, T., and C. Oppenheimer (2015), Extracting high temperature event radiance from satellite images and correcting for saturation using Independent Component Analysis, *Remote Sens. Environ.*, 158, 56–68, doi:10.1016/j.rse.2014.10.023.
- Bayliss, J. D., J. A. Gualtieri, and R. F. Crompton (1998), Analyzing hyperspectral data with independent component analysis, In 26th AIPR Workshop: Exploiting New Image Sources and Sensors, pp. 133–143, International Society for Optics and Photonics, doi:10.1117/12.300050.
- Beauducel, F., P. Briole, and J. L. Froger (2000), Volcano-wide fringes in ERS synthetic aperture radar interferograms of Etna (1992–1998): Deformation or tropospheric effect?, *J. Geophys. Res.*, 105, 16,391–16,402, doi:10.1029/2000JB900095.
- Beckmann, C. F., and S. M. Smith (2004), Probabilistic independent component analysis for functional magnetic resonance imaging, *IEEE Trans. Med. Imaging*, 23(2), 137–152, doi:10.1109/TMI.2003.822821.
- Bekaert, D. P. S., A. Hooper, and T. J. Wright (2015), A spatially variable power law tropospheric correction technique for InSAR data, *J. Geophys. Res. Solid Earth*, 120, 1345–1356, doi:10.1002/2014JB011558.
- Bell, A. J., and T. J. Sejnowski (1995), An information-maximization approach to blind separation and blind deconvolution, *Neural Comput.*, 7(6), 1129–1159, doi:10.1162/neco.1995.7.6.1129.
- Biggs, J., S. K. Ebmeier, W. P. Aspinall, Z. Lu, M. E. Pritchard, R. S. J. Sparks, and T. A. Mather (2014), Global link between deformation and volcanic eruption quantified by satellite imagery, *Nat. Commun.*, 5, doi:10.1038/ncomms4471.
- Bürgmann, R., P. A. Rosen, and E. J. Fielding (2000), Synthetic aperture radar interferometry to measure Earth's surface topography and its deformation, *Ann. Rev. Earth Planet. Sci.*, 28(1), 169–209, doi:10.1146/annurev.earth.28.1.169.
- Calhoun, V. D., and T. Adali (2006), Unmixing fMRI with independent component analysis, *IEEE Eng. Med. Biol. Mag.*, 25(2), 79–90, doi:10.1109/EMEMB.2006.1607672.
- Caricchi, L., J. Biggs, C. Annen, and S. K. Ebmeier (2014), The influence of cooling, crystallisation and re-melting on the interpretation of geodetic signals, *Earth Planet. Sci. Lett.*, doi:10.1016/j.epsl.2013.12.002.
- Chaussard, E. (2016), Subsidence in the Parícutin lava field: Causes and implications for interpretation of deformation fields at volcanoes, *J. Volcanol. Geotherm. Res.*, 320, 1–11, doi:10.1016/j.jvolgeores.2016.04.009.
- Comon, P. (1994), Independent component analysis: A new concept?, *Signal Process.*, 36(3), 287–314.



- De Lauro, E., S. De Martino, M. Falanga, and M. Palo (2009), Decomposition of high-frequency seismic wavefield of the Strombolian-like explosions at Erebus volcano by independent component analysis, *Geophys. J. Int.*, 177(3), 1399–1406, doi:10.1111/j.1365-246X.2009.04157.x.
- Doin, M. P., C. Lasserre, G. Peltzer, O. Cavié, and C. Doubre (2009), Corrections of stratified tropospheric delays in SAR interferometry: Validation with global atmospheric models, *J. Appl. Geophys.*, 69(1), 35–50.
- Ebmeier, S. K., J. Biggs, T. A. Mather, and F. Amelung (2013), Applicability of InSAR to tropical volcanoes: Insights from Central America, *Geol. Soc. London Spec. Publ.*, 380(1), 15–37.
- Ebmeier, S. K., J. Biggs, C. Muller, and G. Avaré (2014), Thin-skinned mass-wasting responsible for edifice-wide deformation at Arenal Volcano, *Front. Earth Sci.*, 2, 35, doi:10.3389/feart.2014.00035.
- Elliott, J. R., J. Biggs, B. Parsons, and T. J. Wright (2008), InSAR slip rate determination on the Altyn Tagh Fault, northern Tibet, in the presence of topographically correlated atmospheric delays, *Geophys. Res. Lett.*, 35, L12309, doi:10.1029/2008GL033659.
- Elliott, J. R., R. J. Walters, and T. J. Wright (2016), The role of space-based observation in understanding and responding to active tectonic and earthquakes, *Nat. Commun.*, 7, doi:10.1038/ncomms13844.
- Emardson, T. R., M. Simons, and F. H. Webb (2003), Neutral atmospheric delay in interferometric synthetic aperture radar applications: Statistical description and mitigation, *J. Geophys. Res.*, 108(B5), 2231, doi:10.1029/2002JB001781.
- Esposito, F., T. Scarabino, A. Hyvärinen, J. Himberg, E. Formisano, S. Comani, G. Tedeschi, R. Goebel, E. Seifritz, and F. Di Salle (2005), Independent component analysis of fMRI group studies by self-organizing clustering, *Neuroimage*, 25(1), 193–205, doi:10.1016/j.neuroimage.2004.10.042.
- Farr, T. G., et al. (2007), The shuttle radar topography mission, *Rev. Geophys.*, 45, RG2004, doi:10.1029/2005RG000183.
- Ferretti, A., C. Prati, and F. Rocca (2001), Permanent scatterers in SAR interferometry, *IEEE Trans. Geosci. Remote Sens.*, 39(1), 8–20, doi:10.1109/36.898661.
- Foster, J., B. Brooks, T. Cherubini, C. Shacat, S. Businger, and C. L. Werner (2006), Mitigating atmospheric noise for InSAR using a high resolution weather model, *Geophys. Res. Lett.*, 33, L16304, doi:10.1029/2006GL026781.
- Foster, J., J. Kealy, T. Cherubini, S. Businger, Z. Lu, and M. Murphy (2013), The utility of atmospheric analyses for the mitigation of artifacts in InSAR, *J. Geophys. Res. Solid Earth*, 118, 748–758, doi:10.1002/jgrb.50093.
- Fournier, T. J., M. E. Pritchard, and S. N. Riddick (2010), Duration, magnitude, and frequency of subaerial volcano deformation events: New results from Latin America using InSAR and a global synthesis, *Geochem. Geophys. Geosyst.*, 11, Q01003, doi:10.1029/2009GC002558.
- Fries, C. (1953), Volumes and weights of pyroclastic material, lava, and water erupted by Parícutin volcano, Michoacan, Mexico, *Eos Trans. AGU*, 34(4), 603–616, doi:10.1029/TR034i004p00603.
- González, P. J., K. F. Tiampo, M. Palano, F. Cannavó, and J. Fernández (2012), The 2011 Lorca earthquake slip distribution controlled by groundwater crustal unloading, *Nat. Geosci.*, 5(11), 821–825.
- González, P. J., M. Bagnardi, A. J. Hooper, Y. Larsen, P. Marinkovic, S. V. Samsonov, and T. J. Wright (2015), The 2014–2015 eruption of Fogo volcano: Geodetic modeling of Sentinel-1 TOPS interferometry, *Geophys. Res. Lett.*, 42, 9239–9246, doi:10.1002/2015GL066003.
- Hanssen, R. F. (2001), *Radar Interferometry: Data Interpretation and Error Analysis*, vol. 2, Springer Sci. & Business Media, Netherlands.
- Henderson, S. T., and M. E. Pritchard (2013), Decadal volcanic deformation in the Central Andes Volcanic Zone revealed by InSAR time series, *Geochem. Geophys. Geosyst.*, 14, 1358–1374, doi:10.1002/ggge.20074.
- Hooper, A., P. Segall, and H. Zebker (2007), Persistent scatterer interferometric synthetic aperture radar for crustal deformation analysis, with application to Volcán Alcedo, Galápagos, *J. Geophys. Res.*, 112, B07407, doi:10.1029/2006JB004763.
- Hyvärinen, A. (2013), Independent component analysis: Recent advances, *Phil. Trans. R. Soc. A*, 371(1984), 20110534. doi:10.1098/rsta.2011.0534.
- Hyvärinen, A., and E. Oja (1997), A fast fixed-point algorithm for ICA, *Neural Comput.*, 9, 1483–1492.
- Hyvärinen, A., and E. Oja (2000), Independent component analysis: Algorithms and applications, *Neural Networks*, 13(4), 411–430.
- Hyvärinen, A., and P. Ramkumar (2013), Testing independent component patterns by inter-subject or inter-session consistency, *Front. Human Neurosci.*, 7, 94, doi:10.3389/fnhum.2013.00094.
- Hyvärinen, A., J. Sarela, and R. Vigário (1999), Spikes and bumps: Artefacts generated by independent component analysis with insufficient sample size, In First International Workshop on Independent Component Analysis and Signal Separation.
- Hyvärinen, A., J. Karhunen, and E. Oja (2004), *Independent Component Analysis*, vol. 46, John Wiley, New York.
- Iwamori, H., and F. Albarède (2008), Decoupled isotopic record of ridge and subduction zone processes in oceanic basalts by independent component analysis, *Geochem. Geophys. Geosyst.*, 9, Q04033, doi:10.1029/2007GC001753.
- Jay, J., F. Costa, M. Pritchard, L. Lara, B. Singer, and J. Herrin (2014), Locating magma reservoirs using InSAR and petrology before and during the 2011–2012 Cordón Caulle silicic eruption, *Earth Planet. Sci. Lett.*, 395, 254–266, doi:10.1016/j.epsl.2014.03.046.
- Jolivet, R., R. Grandin, C. Lasserre, M. P. Doin, and G. Peltzer (2011), Systematic InSAR tropospheric phase delay corrections from global meteorological reanalysis data, *Geophys. Res. Lett.*, 38, L17311, doi:10.1029/2011GL048757.
- Jolivet, R., P. S. Agram, N. Y. Lin, M. Simons, M. P. Doin, G. Peltzer, and Z. Li (2014), Improving InSAR geodesy using global atmospheric models, *J. Geophys. Res. Solid Earth*, 119, 2324–2341, doi:10.1002/2013JB010588.
- Liu, B., W. Dai, W. Peng, and X. Meng (2015), Spatiotemporal analysis of GPS time series in vertical direction using independent component analysis, *Earth Planets Space*, 67(1), 189, doi:10.1186/s40623-015-0357-1.
- Lohman, R. B., and M. Simons (2005), Some thoughts on the use of InSAR data to constrain models of surface deformation: Noise structure and data downsampling, *Geochem. Geophys. Geosyst.*, 6(1).
- Lu, Z., and D. Dzurisin (2014), InSAR imaging of Aleutian volcanoes, in *InSAR Imaging of Aleutian Volcanoes*, pp. 87–345, Springer Berlin Heidelberg, doi:10.1007/978-3-642-00348-6\_6.
- Massonnet, D., M. Rossi, C. Carmona, F. Adragna, G. Peltzer, K. Feigl, and T. Rabaute (1993), The displacement field of the Landers earthquake mapped by radar interferometry, *Nature*, 364(6433), 138–142.
- Mogi, K. (1958), Relations between the eruptions of various volcanoes and the deformations of the ground surfaces around them, *Bull. Earthquake Res. Inst.*, 36, 99–134.
- Parker, A. L., J. Biggs, R. J. Walters, S. K. Ebmeier, T. J. Wright, N. A. Teanby, and Z. Lu (2015), Systematic assessment of atmospheric uncertainties for InSAR data at volcanic arcs using large-scale atmospheric models: Application to the Cascade volcanoes, United States, *Remote Sens. Environ.*, 170, 102–114.
- Pinel, V., M. P. Poland, and A. Hooper (2014), Volcanology: Lessons learned from synthetic aperture radar imagery, *J. Volcanol. Geotherm. Res.*, 289, 81–113, doi:10.1016/j.jvolgeores.2014.10.010.
- Poland, M. P., and Z. Lu (2004), Radar interferometry observations of surface displacements during pre-and co-eruptive periods at Mount St. Helens, Washington, 1992–2005. A volcano rekindled: The renewed eruption of Mount St. Helens, 2006.



- Pritchard, M. E., J. A. Jay, F. Aron, S. T. Henderson, and L. E. Lara (2013), Subsidence at southern Andes volcanoes induced by the 2010 Maule, Chile earthquake, *Nat. Geosci.*, **6**, 632–636, doi:10.1038/ngeo1855.
- Remy, D., S. Bonvalot, P. Briole, and M. Murakami (2003), Accurate measurements of tropospheric effects in volcanic areas from SAR interferometry data: Application to Sakurajima volcano (Japan), *Earth Planet. Sci. Lett.*, **213**(3), 299–310.
- Romero, J. E., et al. (2016), Eruption dynamics of the 22–23 April 2015 Calbuco volcano (Southern Chile): Analyzes of tephra fall deposits, *J. Volcanol. Geotherm. Res.*, **317**, 15–29, doi:10.1016/j.jvolgeores.2016.02.027.
- Sigmundsson, F., et al. (2015), Segmented lateral dyke growth in a rifting event at Bardarbunga volcanic system, Iceland, *Nature*, **517**(7533), 191–195, doi:10.1038/nature14111.
- Simons, M. and P. A. Rosen (2007), Interferometric synthetic aperture radar geodesy, in *Treatise on Geophysics - Geodesy*, vol. 3, pp. 391–446, Elsevier, Amsterdam.
- Stone, J. V. (2004), *Independent component analysis*, John Wiley, New York.
- Stone, J. V., J. Porrill, N. R. Porter, and I. D. Wilkinson (2002), Spatiotemporal independent component analysis of event-related fMRI data using skewed probability density functions, *NeuroImage*, **15**(2), 407–421.
- Van Eaton, A. R., A. Amigo, D. Bertin, L. G. Mastin, R. Giacosa, J. González, O. Valderrama, K. Fontijn, and S. A. Behnke (2016), Volcanic lightning and plume behavior reveal evolving hazards during the April 2015 eruption of Calbuco Volcano, Chile, *Geophys. Res. Lett.*, **43**, 3563–3571, doi:10.1002/2016GL068076.
- Wadge, G., A. Costa, K. Pascal, C. Werner, and T. Webb (2016), The variability of refractivity in the atmospheric boundary layer of a tropical island volcano measured by ground-based interferometric radar, *Boundary Layer Meteorol.*, **161**, 309–333, doi:10.1007/s10546-016-0168-3.
- Walters, R. J., Elliott, J. R., Li, Z., and Parsons, B. (2013), Rapid strain accumulation on the Ashkabad fault (Turkmenistan) from atmosphere-corrected InSAR, *J. Geophys. Res. Solid Earth*, **118**, 3674–3690, doi:10.1002/jgrb.50236.
- Wicks, C. W., D. Dzurisin, S. Ingebritsen, W. Thatcher, Z. Lu, and J. Iverson (2002), Magmatic activity beneath the quiescent Three Sisters volcanic center, central Oregon Cascade Range, USA, *Geophys. Res. Lett.*, **29**(7), 1122, doi:10.1029/2001GL014205.
- Zebker, H. A., P. A. Rosen, and S. Hensley (1997), Atmospheric effects in interferometric synthetic aperture radar surface deformation and topographic maps, *J. Geophys. Res.*, **102**(B4), 7547–7563.